



OPEN

Fluvial organic carbon cycling regulated by sediment transit time and mineral protection

Marisa Repasch ^{1,2}✉, Joel S. Scheingross ³, Niels Hovius^{1,2}, Maarten Lupker ⁴, Hella Wittmann ¹, Negar Haghipour^{4,5}, Darren R. Gröcke ⁶, Oscar Orfeo⁷, Timothy I. Eglinton ⁴ and Dirk Sachse ¹

Rivers transfer terrestrial organic carbon (OC) from mountains to ocean basins, playing a key role in the global carbon cycle. During fluvial transit, OC may be oxidized and emitted to the atmosphere as CO₂ or preserved and transported to downstream depositional sinks. The balance between oxidation and preservation determines the amount of particulate OC (POC) that can be buried long term, but the factors regulating this balance are poorly constrained. Here, we quantify the effects of fluvial transit on POC fluxes along an ~1,300 km lowland channel with no tributaries. We show that sediment transit time and mineral protection regulate the magnitude and rate of POC oxidation, respectively. Using a simple turnover model, we estimate that annual POC oxidation is a small percentage of the POC delivered to the river. Modelling shows that lateral erosion into POC-rich floodplains can increase POC fluxes to downstream basins, thereby offsetting POC oxidation. Consequently, rivers with high channel mobility can enhance CO₂ drawdown while management practices that stabilize river channels may reduce the potential for CO₂ drawdown.

Earth's habitability is regulated by atmospheric CO₂ concentrations. Over geologic timescales, silicate weathering and terrestrial organic carbon burial drive atmospheric CO₂ drawdown, while solid Earth degassing and organic carbon oxidation release CO₂ to the atmosphere. Terrestrial organic carbon burial is facilitated by geomorphic processes such as erosion, which removes carbon from the terrestrial biosphere, and fluvial transit, which transfers biospheric particulate organic carbon (POC) to downstream depositional basins^{1,2}. The amount of POC that can be buried long term is modulated by the balance between oxidation and preservation during fluvial transit, including time spent in transient storage in floodplains^{3,4}. Predicting how fluvial transit regulates long-term POC burial, and ultimately atmospheric CO₂ concentrations, requires an understanding of the feedbacks between geomorphic and geochemical processes governing sediment routing and POC decomposition^{5,6}.

We hypothesize that the balance between fluvial POC oxidation and preservation ('POC budget') is controlled primarily by two factors: (1) fluvial transit time and (2) mineral protection of POC. First, fluvial transit time determines the residence time of POC in river systems^{3,7–9}, and longer residence times facilitate POC oxidation. In coastal mountains with short (10¹–10² km), steep rivers linking to the ocean, fluvial POC may be efficiently transferred to depocentres^{8,10}. In continental settings, fluvial transit lengths and times can exceed 10³ km and 20 kyr^{11–13}, respectively, and many large rivers have been characterized as net CO₂ sources due to degassing from channels and floodplains^{14–18}. Where measured, ¹⁴C ages of exported fluvial POC are an order of magnitude younger than clastic sediment transit times, indicating substantial POC turnover during lowland transit^{9,20}. As POC oxidation is probably limited during in-river transport²¹, turnover must occur primarily during transient floodplain storage. However, sediment transit time data are scarce²², making it difficult to quantify the effect of sediment routing on the fluvial carbon budget.

A second possible control on POC turnover is the degree of coupling between clastic sediment and POC as stronger coupling reduces decomposition rates. Fluvial POC may travel as discrete particles or bound to minerals^{9,23,24}. Reactive mineral phases, such as aluminium, iron and manganese oxyhydroxides, may protect organic carbon from microbial degradation^{25–27} via cation-bridging reactions with phyllosilicates²⁸ or ligand exchange on hydroxylated mineral surfaces²⁹. This mineral association reduces POC turnover, and evidence of POC that has aged up to 10⁴ yr^{30–32} suggests that this mechanism can be volumetrically important in river systems. However, the relative importance of organo–mineral complexes for preserving fluvial POC remains unclear³³.

In this article, we trace organic matter through a river system with no tributaries for nearly 1,300 km to quantify the effects of sediment transit time and organo–mineral interactions on the fate of fluvial POC. Using existing fluvial sediment transit time estimates³⁴, POC isotope measurements and secondary mineral data for actively transported sediment, we show that POC oxidation is regulated by both transit time and mineral protection. Our analysis allows us to develop a simple model to estimate POC turnover during fluvial transit, and we use this model to explore the geomorphic and geochemical drivers of fluvial organic carbon cycling.

A natural flume experiment

The Rio Bermejo in northern Argentina (Fig. 1) drains eastward from the Andes, delivering ~103 Mt yr⁻¹ of sediment to the lowland basin³⁴, ~92% of which is transported during the South American monsoon season (December–May) (Extended Data Fig. 1). The river flows ~1,270 km from the last tributary confluence at the mountain front (Rio San Francisco, river km 0) to the Rio Paraguay, with no notable tributaries, limited anthropogenic activity and negligible aquatic productivity due to high flow velocity and turbidity³⁵ (Extended Data Fig. 2).

¹German Research Centre for Geosciences (GFZ), Potsdam, Germany. ²Institute of Geosciences, University of Potsdam, Potsdam, Germany. ³Department of Geological Sciences and Engineering, University of Nevada Reno, Reno, NV, USA. ⁴Geological Institute, ETH Zürich, Zürich, Switzerland. ⁵Laboratory of Ion Beam Physics, ETH Zürich, Zürich, Switzerland. ⁶Department of Earth Sciences, Durham University, Durham, UK. ⁷CONICET, Center for Applied Ecology of the Littoral, Universidad Nacional de Nordeste, Corrientes, Argentina. ✉e-mail: repasch1@llnl.gov

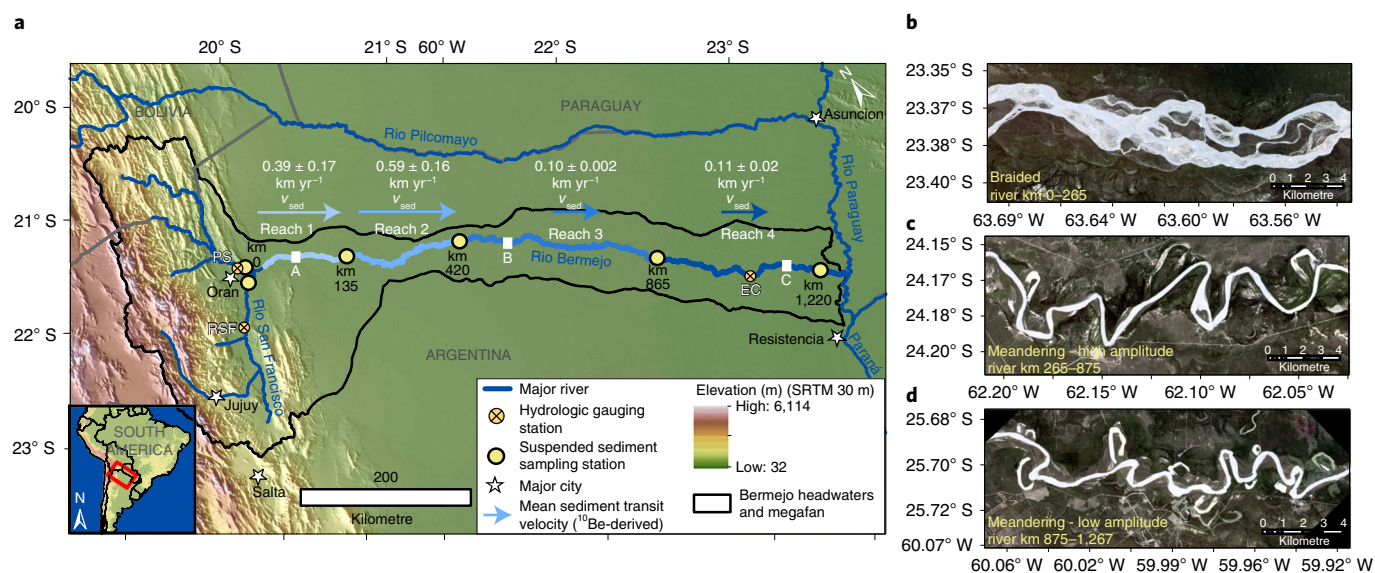


Fig. 1 | Overview of Rio Bermejo study area. a, Topographic map of the Rio Bermejo system. Blue arrows show v_{sed} (km yr⁻¹) for four reaches between sampling points. v_{sed} was determined for each reach from the measured accumulation of meteoric ¹⁰Be between upstream and downstream sampling points³⁴. **b–d**, Planet satellite images showing differences in morphology along the channel (downloaded from <https://api.planet.com/>) for river km 0–265 (**b**), river km 265–875 (**c**) and river km 875–1,267 (**d**). SRTM, Shuttle Radar Topography Mission.

From river km 0 to km 265, the river is braided and perched above the flood basin. The remaining ~1,000 km is a single-thread, meandering channel that migrates up to 30 m yr⁻¹ (ref. ³⁴) (Fig. 1). While water can transit this system in ~14 days, sediment requires on average ~8,500 years, as determined by the net accumulation of ¹⁰Be in river sediment between river km 0 and 1,220 (ref. ³⁴). As a result of lateral channel migration, sediment experiences on average ~4.5 deposition–erosion episodes during lowland transit, each taking ~1,900 years (ref. ³⁴). Averaged across all particle sizes, the downstream sediment transit velocity (v_{sed}) is ~0.15 km yr⁻¹. Due to local differences in channel morphodynamics, v_{sed} varies along the channel, from ~0.59 km yr⁻¹ in the braided reach to ~0.1 km yr⁻¹ in the lower meandering reach (Fig. 1). In the following, we show that v_{sed} is a first-order control on POC oxidation during fluvial transit.

Downstream evolution of POC composition

To evaluate how POC evolves during fluvial transit, we measured POC concentrations, stable (¹³C/¹²C) and radioactive (¹⁴C) carbon isotopes and mineral specific surface area (SSA) of suspended sediment sampled from river depth profiles at six stations during monsoon season (Methods). To account for hydrodynamic sorting and characterize the bulk composition of the suspended load, we depth-integrated each profile, weighting individual sample measurements by suspended sediment and POC concentrations (Supplementary Table 1). At river km 0, the depth-integrated POC concentration (POC_{DI}) was $0.18 \pm 0.06\%$. Assuming POC_{DI} is constant during monsoon season and dry season changes are negligible, the mean annual headwater POC flux (Q_{hw}) is $1.85 \pm 0.62 \times 10^5 \text{ tC yr}^{-1}$ (Methods). At river km 1,220, POC_{DI} increased to $0.28 \pm 0.02\%$, yielding a mean annual POC export of $2.24 \pm 0.16 \times 10^5 \text{ tC yr}^{-1}$ (Q_{out}). The difference between Q_{hw} and Q_{out} is $+0.39 \times 10^5 \text{ tC yr}^{-1}$, suggesting that, under modern conditions, lateral POC inputs exceed POC lost during transit.

POC_{DI} increased along the river's braided reach to $0.30 \pm 0.04\%$, while OC loading (mass of POC per unit SSA) remained constant at 0.21–0.23 mgCm⁻² (Fig. 2 and Supplementary Table 1). These diverging trends probably arise from selective deposition of coarse sediment with low POC (Extended Data Fig. 3). The OC loading

decreased significantly in the meandering reach to ~0.13 mgCm⁻² due to lateral erosion of weathered floodplain sediment with high SSA. We further explored downstream POC transformations using stable and radiocarbon isotope measurements.

The POC stable carbon isotope composition ($\delta^{13}\text{C}_{\text{POC}}$) for individual samples ranged from -27.3‰ to -24.9‰ , and radiocarbon content (expressed as fraction modern, $F^{14}\text{C}_{\text{POC}}$) ranged from 0.78 to 0.94 (Fig. 2). All $\delta^{13}\text{C}_{\text{POC}}$ and $F^{14}\text{C}_{\text{POC}}$ values were within the compositional range of regional topsoil, vegetation and floodplain sediment (Fig. 2 and Extended Data Table 1), indicating that fluvial POC comprises a mixture of compounds ranging in age and turnover time. This is supported by $F^{14}\text{C}$ values of refractory terrestrial leaf wax *n*-alkanes ($F^{14}\text{C}_{\text{alk}}$) in river sediment. $F^{14}\text{C}_{\text{alk}}$ ranged from 0.74 to 0.86, significantly lower than $F^{14}\text{C}_{\text{POC}}$ values for the same samples, suggesting that a fraction of fluvial POC derives from an older, preferentially preserved POC pool³⁶.

Within depth profiles, surface-water samples generally had higher POC concentrations, more positive $\delta^{13}\text{C}_{\text{POC}}$ values and lower $F^{14}\text{C}_{\text{POC}}$ values than samples collected >0.5 m below the surface (Fig. 2). In agreement, $F^{14}\text{C}_{\text{alk}}$ values were generally lower for surface samples. These compositional differences reflect hydrodynamic sorting^{33,37}, where water-logged plant dominated POC at depth, and surface-water samples were concentrated in ¹³C-enriched POC associated with low-density mineral phases^{25,26,38}. With increasing transit distance along the meandering segment, surface-water POC became consistently more ¹³C enriched and ¹⁴C depleted, reflecting progressive addition of aged, mineral-associated POC. Bedload samples had low POC concentrations (Supplementary Table 1), suggesting that vertical exchange between bedload and suspended load has negligible effects on depth-integrated POC composition.

From river km 135 to 420, where v_{sed} was highest, $\delta^{13}\text{C}_{\text{DI}}$ remained constant, but $F^{14}\text{C}_{\text{DI}}$ increased from 0.83 to 0.92 (¹⁴C-age decrease of ~780 years) (Fig. 2). This may reflect mass loss of ¹⁴C-depleted sediment through selective deposition of coarse sand (including lithic fragments and petrogenic POC) and/or fresh organic matter addition. From river km 420 to 1,220, where v_{sed} is low, $\delta^{13}\text{C}_{\text{DI}}$ values increased from $-26.4 \pm 0.3\text{‰}$ to $-25.5 \pm 0.3\text{‰}$, and $F^{14}\text{C}_{\text{DI}}$ values decreased from 0.92 to 0.86 (~510 years ¹⁴C-age increase).

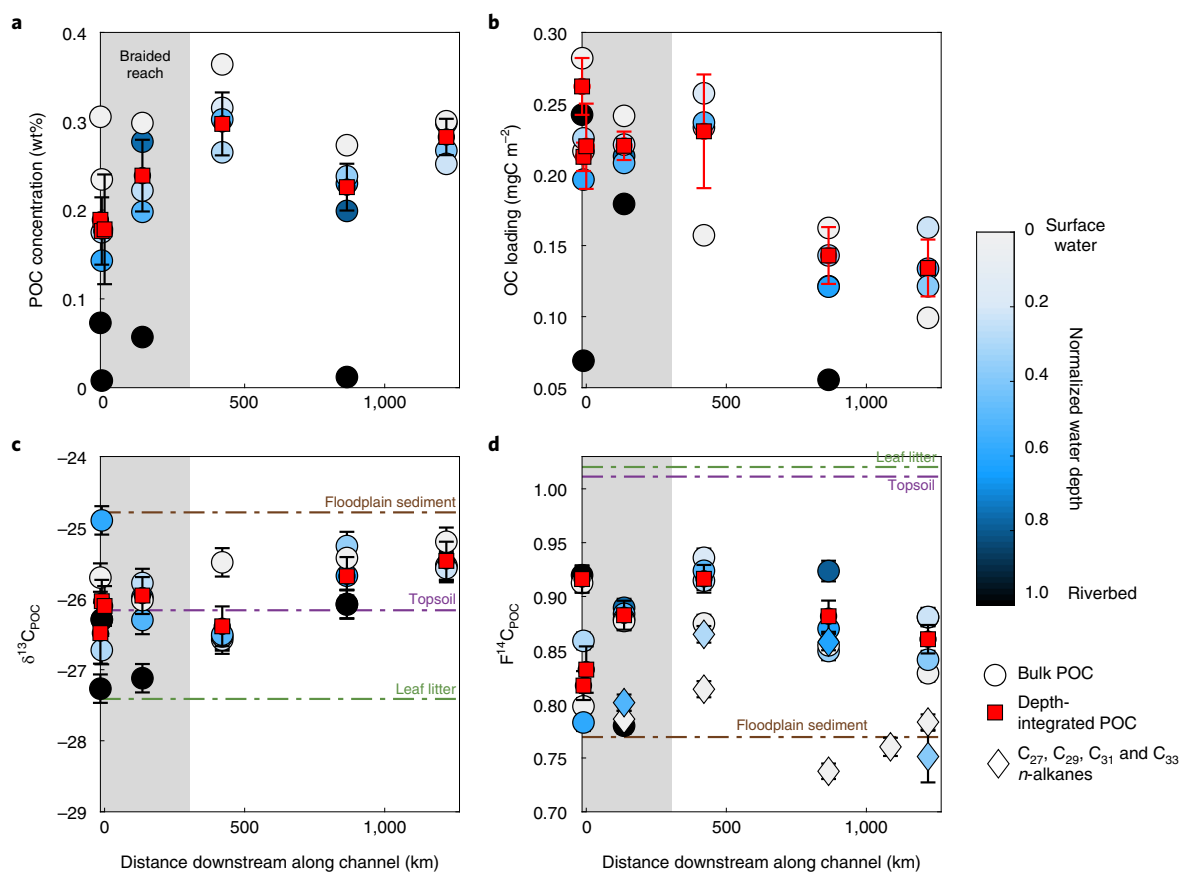


Fig. 2 | Downstream evolution of fluvial POC composition. **a–d**, POC concentration (**a**), OC loading (**b**), $\delta^{13}\text{C}_{\text{POC}}$ (**c**) and $F^{14}\text{C}_{\text{POC}}$ and $F^{14}\text{C}_{\text{alk}}$ (**d**) measurements for samples collected from depth profiles along the Rio Bermejo. Distance 0 represents the last tributary confluence at the mountain front. Circles/diamonds are individual samples coloured by depth in water column relative to total flow depth, with error bars representing analytical precision. Red squares are depth-integrated values for each depth profile, with error bars representing standard error of the weighted mean. Dashed horizontal lines indicate mean isotopic values for floodplain sediment⁴⁰, leaf litter and topsoil in the catchment.

These changes probably reflect entrainment of aged, ¹³C-enriched POC from floodplain deposits. These data are consistent with the idea that the time allowed for POC aging and transformation, as captured by sediment transit time, exerts a strong control over POC composition.

Complete POC turnover during floodplain storage would cause $F^{14}\text{C}$ values to increase downstream. The ¹³C-enrichment and apparent POC aging trends along the meandering reach (Fig. 2) suggest that some POC is preserved during floodplain storage, surviving multiple episodes of deposition and erosion. Below, we test the hypothesis that mineral protection limits POC turnover during fluvial transit^{24,28}.

Organo-metal complexation slows POC decomposition

To test whether organo-metal complexation slows POC turnover during fluvial transit, we measured acid-extractable metal concentrations in suspended sediment (Methods) as proxies for the abundance of reactive oxyhydroxide phases³⁹. Extractable [Al], [Fe], [Mg], [Mn] and SSA showed statistically significant correlations with $F^{14}\text{C}_{\text{POC}}$ (negative), $F^{14}\text{C}_{\text{alk}}$ (negative) and $\delta^{13}\text{C}_{\text{POC}}$ (positive) (Fig. 3 and Extended Data Figs. 4 and 5). Samples with higher metal concentrations contained relatively older, ¹³C-enriched POC. All correlations between $F^{14}\text{C}_{\text{POC}}$ and metal concentrations are stronger than the correlation between $F^{14}\text{C}_{\text{POC}}$ and SSA, suggesting that organic compounds are not only adsorbed onto mineral surfaces but also bound to secondary minerals via complexation reactions²⁹. The ¹³C enrichment of mineral-stabilized POC may result

from decomposition in the floodplain⁴⁰ and/or preferential reaction of minerals with ¹³C-enriched organic compounds^{25,41}. These data suggest that organo-mineral complexes developed during transient floodplain storage help stabilize biospheric POC (POC_{bio}), in agreement with our hypothesis, and can therefore increase the probability of long-term POC_{bio} burial.

A model for POC oxidation during fluvial transit

Our data provide evidence for POC oxidation, fluvial recruitment of young biomass via lateral channel migration and POC preservation by organo-mineral complexation during fluvial transit. In the following we use these findings to estimate the POC budget of the Rio Bermejo, as regulated by sediment transit time and mineral protection.

We calculated the annual Rio Bermejo POC oxidation flux by defining a relationship between v_{sed} and POC decomposition rate. We assume that POC travels with clastic sediment at v_{sed} because we found water-logged plant organic matter at all water depths, and POC reactivity is described by a decomposition rate constant (k , 1 yr⁻¹) (Methods). Linking v_{sed} and k , the characteristic channel length (x_c) over which the fluvial POC load is turned over (depleted) is:

$$x_c = \frac{v_{\text{sed}}}{k} \quad (1)$$

Then the number of POC turnover cycles (n_c) during transit along a river system of length L is:

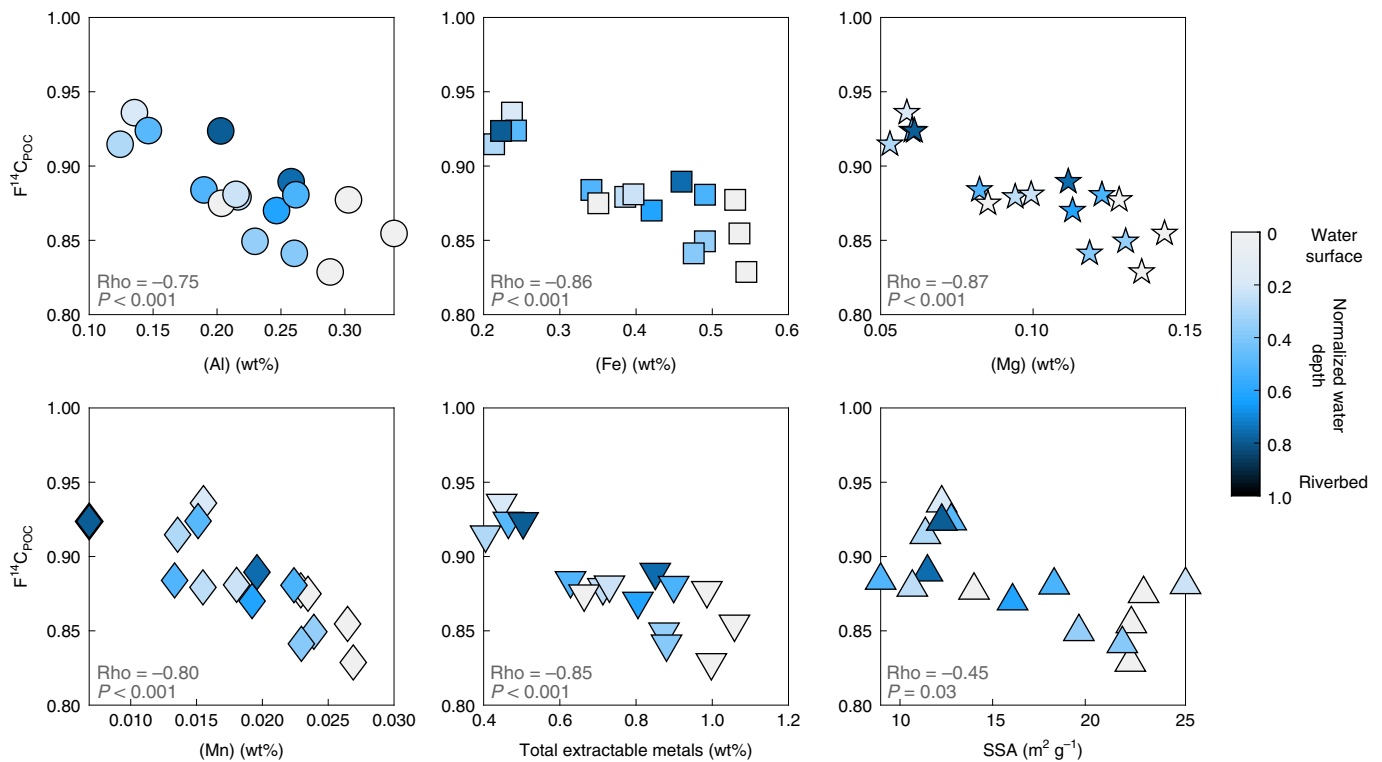


Fig. 3 | Evidence for organo-mineral associations. Concentrations of acid-extractable metal ions Al, Fe, Mg, Mn, total extractable metals and mineral SSA versus $F^{14}C_{POC}$ of river suspended sediment (excluding bedload). Colour scale indicates the normalized sample depth in the water column. Rho is the Pearson linear correlation coefficient and the P value indicates the statistical significance of those correlations.

$$n_c = \frac{L}{x_c} \quad (2)$$

Finally, the annual POC oxidation flux (Q_{ox}) resulting from fluvial transit of the mean annual headwater POC load (POC_{in} , tC) over transit time t is:

$$Q_{ox} = \frac{n_c \times POC_{in}}{t} \quad (3)$$

We assume geomorphic steady state, where mean POC_{in} and v_{sed} are constant over $\sim 10^4$ yr transit timescales. This also assumes POC_{in} is spatially constant, such that we underestimate POC oxidation if the POC load increases in downstream reaches. Fluvial POC contains numerous carbon pools ranging in source, age and decomposition rate^{4,23,42,43}. For simplicity, we divided fluvial POC into two pools: (1) fast-cycling discrete organic particles, POC_{fast} , and (2) slow-cycling mineral-associated POC, POC_{slow} ^{22,32}. We assume each POC pool is homogeneous and decomposition rates are constant, although this is rarely the case in nature⁴⁴.

Annually, the Rio Bermejo receives $\sim 1.85 \times 10^5$ tC POC via erosion in the headwaters (POC_{in}). According to a Bayesian endmember isotope mixing model, $47\% \pm 10\%$ of this load behaves as POC_{slow} and $53\% \pm 17\%$ as POC_{fast} (Methods and Extended Data Table 2). For these two pools, we estimated k using radiocarbon data, following Torn et al.⁴⁵ (Methods). For POC_{fast} , we set the turnover time to ~ 17 years, which is the modelled ecosystem turnover time in the subtropical Rio Bermejo region⁴⁶, yielding $k_{fast} \approx 6 \times 10^{-2} yr^{-1}$ (Methods and Extended Data Table 3). For k_{slow} , we utilized n -alkane $F^{14}C_{alk}$ data because of their recalcitrance and association with secondary minerals³⁶. As a conservative estimate of POC_{slow} oxidation, we used the lowest $F^{14}C_{alk}$ value (0.74), yielding $k_{slow} \approx 3.4 \times 10^{-4} yr^{-1}$ (turnover time of $\sim 2,900$ years) (Methods).

Using equations (1–3), we estimated separate oxidation fluxes for POC_{slow} and POC_{fast} during an 8,500 yr fluvial transit along the $\sim 1,270$ km lowland Rio Bermejo (Methods). POC turnover varies significantly along the Rio Bermejo (Extended Data Table 4). With lower transit velocity (increased storage time), the meandering reach is the locus of turnover, with a POC turnover length scale (x_c) nearly an order of magnitude shorter than in the braided reach (Fig. 4). This highlights the control of channel morphodynamics on the fate of POC in lowland rivers.

Along the full channel length, x_c for POC_{fast} is 2 ± 1 km, resulting in n_c of 520 ± 160 (Fig. 4). By contrast, x_c for POC_{slow} is 430 ± 190 km, resulting in n_c of 3.0 ± 0.9 . Since the Rio Bermejo sediment load experiences ~ 4.5 deposition–erosion cycles along this pathway³⁴, POC_{slow} must be coupled to the clastic sediment trajectory, while POC_{fast} is decoupled from it. During $\sim 8,500$ yr transit between the mountain front and Rio Paraguay, turnover results in Q_{ox} of $30.4 (+23.8/-17.0)$ tC yr⁻¹ for POC_{slow} and $6,050 (+4410/-3210)$ tC yr⁻¹ for POC_{fast} , suggesting that ~ 2 – 6% of POC_{in} is oxidized annually during fluvial transit.

Controls on the fluvial POC budget

Our data show that sediment transit time and mineral protection are primary controls on the fate of fluvial POC during source-to-sink transit. Our model for POC turnover allows quantification of the respective roles of these two governing mechanisms. Here we define a transit time-dependent fluvial POC budget:

$$Q_{out} - Q_{hw} = Q_{lat} - \frac{(n_c \times f_{slow} \times POC_{in})_{slow} + (n_c \times f_{fast} \times POC_{in})_{fast}}{t} \quad (4)$$

The last term on the right side of equation (4) represents the total annual POC Q_{ox} , encompassing POC_{slow} and POC_{fast} turnover

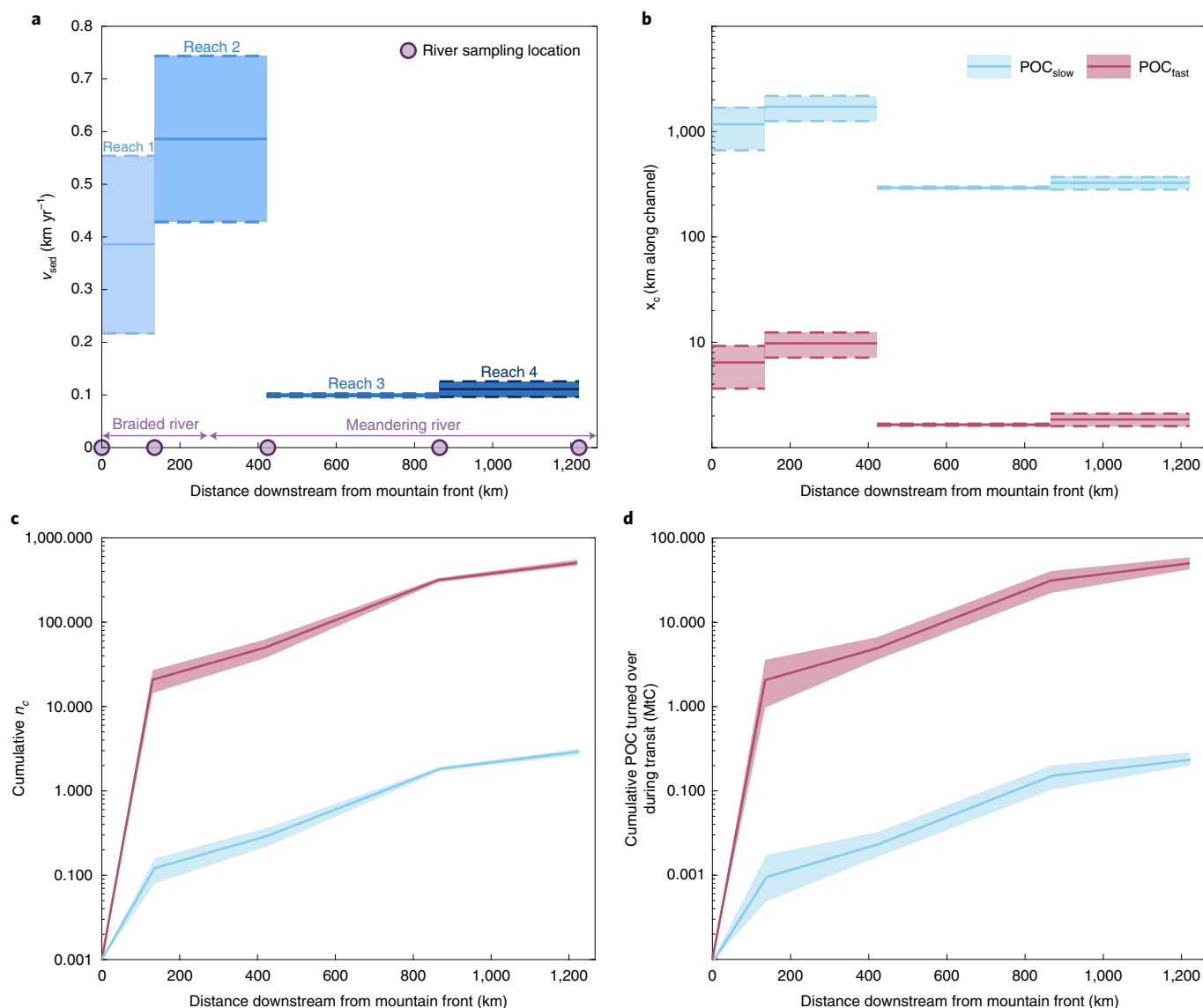


Fig. 4 | Variability in v_{sed} and POC turnover along the channel. **a**, Mean v_{sed} for the four study reaches bound by the sediment sampling locations. **b**, x_c for the four study reaches. **c**, Cumulative n_c that occur during transit along the Rio Bermejo. **d**, Cumulative amount of POC oxidized during transit along the river. All are plotted against distance downstream along the channel from the last tributary confluence at the Andean mountain front. Bold lines represent mean values, and shaded areas represent the range of uncertainty.

during transit, where f is the fraction of POC_{slow} or POC_{fast} contributing to POC_{in}. Q_{lat} represents POC delivered via tributaries or lateral erosion. Whether $Q_{out} - Q_{hw}$ is positive or negative determines whether fluvial transit results in net CO₂ drawdown or release, respectively. Our estimates for the Rio Bermejo, Q_{out} ($\sim 2.24 \times 10^5$ tC yr⁻¹) $>$ Q_{hw} ($\sim 1.85 \times 10^5$ tC yr⁻¹), suggest that additional POC is sequestered from the floodplain during transit. Given Q_{ox} is estimated at $\sim 6.08 \times 10^3$ tC yr⁻¹, equation (4) can be solved for $Q_{lat} \approx 4.58 \times 10^4$ tC yr⁻¹, resulting from lateral erosion into floodplain forests. This agrees with estimates from measured channel migration rates and net primary productivity (Methods). Q_{lat} is nearly an order of magnitude greater than Q_{ox} , more than offsetting oxidative POC loss.

Using equation (4), we test the sensitivity of the fluvial POC budget by varying environmental boundary conditions for the Rio Bermejo. Q_{ox} is linearly proportional to v_{sed} and k (equations (2–4)). Holding all else constant, decreasing v_{sed} by an order of magnitude (mean transit time of ~ 85 kyr) would increase Q_{ox} by an order of magnitude, but such a long transit time is unrealistic for

this system. Removing mineral protection (100% POC_{fast}) would increase Q_{ox} by one order of magnitude, reducing the potential for long-term burial. Doubling k for POC_{fast} would result in net CO₂ release, but such high decomposition rates are realistic only under warmer and wetter conditions. These tests suggest that modern conditions in the Rio Bermejo do not cause significant oxidation relative to the amount of POC exported annually. Drastic changes in boundary conditions are required to oxidize more POC than is preserved. However, the key variables here are linked in complex ways by climate, hydrology, vegetation, tectonics and even anthropogenic disturbance¹⁷, and associated feedbacks may be important.

At a global scale, v_{sed} and k vary across different climatic and tectonic settings. Using equations (1–4), we estimated carbon budgets for the Amazon (tropics) and Mackenzie (Arctic) rivers, where Q_{out} , k and v_{sed} are known. In the Amazon, where POC_{fast} turnover is fast, < 10 years (refs. 18,46), and v_{sed} is ~ 0.21 km yr⁻¹ (ref. 48), $\sim 13\%$ of the POC load is oxidized, but $Q_{lat} > 1$ MtC yr⁻¹ augments POC export to

the ocean. In the Mackenzie River, where POC_{fast} turnover is slow, >70 years (ref. ⁴⁶), and v_{sed} is $\sim 0.09 \text{ km yr}^{-1}$, $<1\%$ of the POC load is oxidized, indicating efficient source-to-sink transit and potential CO_2 drawdown on burial in the Beaufort Sea⁴⁹. These analyses suggest that lateral erosion into vegetated floodplains enhances CO_2 drawdown if POC recruited from the lowlands is buried long term. River engineering, particularly the construction of artificial levees and groins that reduce lateral mobility, can significantly reduce Q_{lat} (ref. ⁴⁷), thereby decreasing potential CO_2 drawdown. Dams may also increase POC oxidation by increasing source-to-sink transit times. Applying this model to rivers globally may yield more robust estimates of river–atmosphere carbon fluxes, advancing our understanding of the global carbon cycle.

Online content

Any methods, additional references, Nature Research reporting summaries, source data, extended data, supplementary information, acknowledgements, peer review information; details of author contributions and competing interests; and statements of data and code availability are available at <https://doi.org/10.1038/s41561-021-00845-7>.

Received: 3 August 2020; Accepted: 21 September 2021;

Published online: 28 October 2021

References

- Hilton, R. G. Climate regulates the erosional carbon export from the terrestrial biosphere. *Geomorphology* **277**, 118–132 (2017).
- Galy, V., Peucker-Ehrenbrink, B. & Eglinton, T. Global carbon export from the terrestrial biosphere controlled by erosion. *Nature* **521**, 204–207 (2015).
- Leithold, E. L., Blair, N. E. & Wegmann, K. W. Source-to-sink sedimentary systems and global carbon burial: a river runs through it. *Earth Sci. Rev.* **153**, 30–42 (2016).
- Galy, V. & Eglinton, T. Protracted storage of biospheric carbon in the Ganges–Brahmaputra basin. *Nat. Geosci.* **4**, 843–847 (2011).
- Clark, K. E. et al. Erosion of organic carbon from the Andes and its effects on ecosystem carbon dioxide balance. *J. Geophys. Res. Biogeosci.* **122**, 449–469 (2017).
- Hilton, R. G. & West, A. J. Mountains, erosion and the carbon cycle. *Nat. Rev. Earth Environ.* **1**, 284–299 (2020).
- Lyons, W. B., Nezat, C. A., Carey, A. E. & Hicks, D. M. Organic carbon fluxes to the ocean from high-standing islands. *Geology* **30**, 443–446 (2002).
- Hilton, R. G., Galy, A., Hovius, N., Hornig, M. J. & Chen, H. Efficient transport of fossil organic carbon to the ocean by steep mountain rivers: an orogenic carbon sequestration mechanism. *Geology* **39**, 71–74 (2011).
- Bouchez, J. et al. Source, transport and fluxes of Amazon River particulate organic carbon: insights from river sediment depth-profiles. *Geochim. Cosmochim. Acta* **133**, 280–298 (2014).
- Bianchi, T. S. et al. Centers of organic carbon burial and oxidation at the land–ocean interface. *Org. Geochem.* **115**, 138–155 (2018).
- Dosseto, A., Bourdon, B. & Turner, S. P. Uranium-series isotopes in river materials: insights into the timescales of erosion and sediment transport. *Earth Planet. Sci. Lett.* **265**, 1–17 (2008).
- Granet, M., Chabaux, F., Stille, P., France-Lanord, C. & Pelt, E. Time-scales of sedimentary transfer and weathering processes from U-series nuclides: clues from the Himalayan rivers. *Earth Planet. Sci. Lett.* **261**, 389–406 (2007).
- Torres, M. A., Kemeny, P. C., Lamb, M. P., Cole, T. L. & Fischer, W. W. Long-term storage and age-biased export of fluvial organic carbon: field evidence from west Iceland. *Geochim. Geophys. Geosyst.* **21**, e2019GC008632 (2020).
- Cole, J. J. & Caraco, N. F. Carbon in catchments: connecting terrestrial carbon losses with aquatic metabolism. *Mar. Freshw. Res.* **52**, 101–110 (2001).
- Battin, T. J. et al. Biophysical controls on organic carbon fluxes in fluvial networks. *Nat. Geosci.* **1**, 95–101 (2008).
- Aufdenkampe, A. K. et al. Riverine coupling of biogeochemical cycles between land, oceans, and atmosphere. *Front. Ecol. Environ.* **9**, 53–60 (2011).
- Raymond, P. A. et al. Global carbon dioxide emissions from inland waters. *Nature* **503**, 355–359 (2013).
- Mayorga, E. et al. Young organic matter as a source of carbon dioxide outgassing from Amazonian rivers. *Nature* **436**, 538–541 (2005).
- Quay, P. D. et al. Carbon cycling in the Amazon River: implications from the ^{13}C compositions of particles and solutes. *Limnol. Oceanogr.* **37**, 857–871 (1992).
- Hedges, J. I. et al. Organic carbon-14 in the Amazon River system. *Science* **231**, 1129–1131 (1986).
- Scheingross, J. S. et al. Preservation of organic carbon during active fluvial transport and particle abrasion. *Geology* **47**, 958–962 (2019).
- Torres, M. A. et al. Model predictions of long-lived storage of organic carbon in river deposits. *Earth Surf. Dynam.* **5**, 711–730 (2017).
- Rosenheim, B. E. & Galy, V. Direct measurement of riverine particulate organic carbon age structure. *Geophys. Res. Lett.* **39**, L19703 (2012).
- Hemingway, J. D. et al. Mineral protection regulates long-term global preservation of natural organic carbon. *Nature* **570**, 228–231 (2019).
- Lalonde, K., Mucci, A., Ouellet, A. & Gélinas, Y. Preservation of organic matter in sediments promoted by iron. *Nature* **483**, 198–200 (2012).
- Johnson, K. et al. Towards a mechanistic understanding of carbon stabilization in manganese oxides. *Nat. Commun.* **6**, 7628 (2015).
- Wagai, R. & Mayer, L. M. Sorptive stabilization of organic matter in soils by hydrous iron oxides. *Geochim. Cosmochim. Acta* **71**, 25–35 (2007).
- Blattmann, T. M. et al. Mineralogical control on the fate of continentally derived organic matter in the ocean. *Science* **366**, 742–745 (2019).
- Kleber, M., Sollins, P. & Sutton, R. A conceptual model of organo–mineral interactions in soils: self-assembly of organic molecular fragments into zonal structures on mineral surfaces. *Biogeochemistry* **85**, 9–24 (2007).
- Drenzek, N. J., Montluçon, D. B., Yunker, M. B., Macdonald, R. W. & Eglinton, T. I. Constraints on the origin of sedimentary organic carbon in the Beaufort Sea from coupled molecular ^{13}C and ^{14}C measurements. *Mar. Chem.* **103**, 146–162 (2007).
- Feng, X. et al. ^{14}C and ^{13}C characteristics of higher plant biomarkers in Washington margin surface sediments. *Geochim. Cosmochim. Acta* **105**, 14–30 (2013).
- French, K. L. et al. Millennial soil retention of terrestrial organic matter deposited in the Bengal Fan. *Sci. Rep.* **8**, 11997 (2018).
- Galy, V., France-Lanord, C. & Lartiges, B. Loading and fate of particulate organic carbon from the Himalaya to the Ganga–Brahmaputra delta. *Geochim. Cosmochim. Acta* **72**, 1767–1787 (2008).
- Repasch, M. et al. Sediment transit time and floodplain storage dynamics in alluvial rivers revealed by meteoric ^{10}Be . *J. Geophys. Res. Earth Surf.* **125**, e2019JF005419 (2020).
- Pedrozo, F. & Bonetto, C. Nitrogen and phosphorus transport in the Bermejo River (South America). *Rev. Hydrobiol. Trop.* **20**, 91–99 (1987).
- van der Voort, T. S. et al. Diverse soil carbon dynamics expressed at the molecular level. *Geophys. Res. Lett.* **44**, 11840–11850 (2017).
- Yu, M. et al. Molecular isotopic insights into hydrodynamic controls on fluvial suspended particulate organic matter transport. *Geochim. Cosmochim. Acta* **262**, 78–91 (2019).
- Wedin, D. A., Tieszen, L. L., Dewey, B. & Pastor, J. Carbon isotope dynamics during grass decomposition and soil organic matter formation. *Ecology* **76**, 1383–1392 (1995).
- Rasmussen, C. et al. Beyond clay: towards an improved set of variables for predicting soil organic matter content. *Biogeochemistry* **137**, 297–306 (2018).
- Scheingross, J. S. et al. The fate of fluvially-deposited organic carbon during transient floodplain storage. *Earth Planet. Sci. Lett.* **561**, 116822 (2021).
- Mikutta, R., Kleber, M., Torn, M. S. & Jahn, R. Stabilization of soil organic matter: association with minerals or chemical recalcitrance? *Biogeochemistry* **77**, 25–56 (2006).
- Marwick, T. R. et al. The age of river-transported carbon: a global perspective. *Glob. Biogeochem. Cycles* **29**, 122–137 (2015).
- Feng, X. et al. Differential mobilization of terrestrial carbon pools in Eurasian Arctic river basins. *Proc. Natl Acad. Sci. USA* **110**, 14168–14173 (2013).
- Sierra, C. A., Müller, M., Metzler, H., Manzoni, S. & Trumbore, S. E. The muddle of ages, turnover, transit, and residence times in the carbon cycle. *Glob. Change Biol.* **23**, 1763–1773 (2017).
- Torn, M. S., Swanston, C. W., Castanha, C. & Trumbore, S. E. Storage and Turnover of Organic Matter in Soil. in *Storage and Turnover of Organic Matter in Soil* (eds. Senesi, N., Xing, B. & Huang, P. M.) (John Wiley & Sons, Inc., 2009).
- Carvalho, N. et al. Global covariation of carbon turnover times with climate in terrestrial ecosystems. *Nature* **514**, 213–217 (2014).
- Wohl, E., Hall, R. O., Lininger, K. B., Sutfin, N. A. & Walters, D. M. Carbon dynamics of river corridors and the effects of human alterations. *Ecol. Monogr.* **87**, 379–409 (2017).
- Dosseto, A., Bourdon, B., Gaillardet, J., Allègre, C. J. & Filizola, N. Time scale and conditions of weathering under tropical climate: study of the Amazon basin with U-series. *Geochim. Cosmochim. Acta* **70**, 71–89 (2006).
- Hilton, R. G. et al. Erosion of organic carbon in the Arctic as a geological carbon dioxide sink. *Nature* **524**, 84–87 (2015).

Publisher's note Springer Nature remains neutral with regard to jurisdictional claims in published maps and institutional affiliations.



Open Access This article is licensed under a Creative Commons Attribution 4.0 International License, which permits use, sharing, adaptation, distribution and reproduction in any medium or format, as long as you give appropriate credit to the original author(s) and the source, provide a link to the Creative Commons license, and indicate if changes were made. The images or other

third party material in this article are included in the article's Creative Commons license, unless indicated otherwise in a credit line to the material. If material is not included in the article's Creative Commons license and your intended use is not permitted by statutory regulation or exceeds the permitted use, you will need to obtain permission directly from the copyright holder. To view a copy of this license, visit <http://creativecommons.org/licenses/by/4.0/>.

© The Author(s) 2021

Methods

River sediment sampling. We collected 24 river suspended sediment samples from the Rio Bermejo between 13 and 25 March 2017, during the peak of the South American monsoon season (December to May), with 75th–85th percentile water discharge conditions (over a 50 yr gauging record) (673 to $1,079$ $\text{m}^3 \text{s}^{-1}$) (Argentina National System of Hydrologic Information, <https://snih.hidricosargentina.gob.ar/>). Suspended sediment flux data indicate that 92% of the annual suspended sediment load is transported during monsoon season, suggesting our samples are representative of the majority of POC transported by the Rio Bermejo. We sampled river water from depth profiles (two to five sampling depths depending on total water depth) at four locations along the mainstem Rio Bermejo, one location on the Rio Bermejo 10 km upstream of the Rio San Francisco confluence, and one location on the Rio San Francisco 15 km upstream from the confluence (Fig. 1). River water was sampled by boat using a weighted eight-litre horizontal sampling bottle. Sediment was recovered by filtering the water under pressure through 0.22 μm polyethersulfone filter paper in a custom filtration device. Four bedload samples were collected with a weighted mesh net. Sediment was dried in an oven at 40°C and subsequently disaggregated and homogenized with mortar and pestle. Suspended sediment concentrations were calculated as dry sediment mass normalized by the sampled water volume.

POC concentrations and isotope measurements. For bulk organic carbon analyses, sediment samples were powdered in a disc mill, and inorganic carbon was removed following Galy et al.⁵⁰. Sediment was decarbonated by leaching in 4% HCl solution, discarding the supernatant, rinsing with deionized water and drying before measurement. Total organic carbon (TOC_{POC}) and $\delta^{13}\text{C}_{\text{POC}}$ were measured in duplicate at Durham University using a Costech elemental analyser (EA) coupled to a CONFLO III and Thermo Scientific Delta V Advantage isotope ratio mass spectrometer. Radiocarbon content was measured using an EA coupled to an accelerator mass spectrometer (EA-AMS) at ETH Zürich⁵¹. We report ^{14}C content as $F^{14}\text{C}_{\text{POC}}$ by normalizing measurements to 95% of the 1950 NBS Oxalic Acid II standard ($\delta^{13}\text{C} = -17.8\text{‰}$) and correcting for mass-dependent fractionation using a common $\delta^{13}\text{C}$ value of -25‰ .

Grain size and SSA measurements. Grain size distributions were measured on ~ 10 mg aliquots of river sediment using a Horiba LA-950 laser particle size analyser. Before measurement, we added 1.5 ml sodium metaphosphate dispersion agent to each sample and shook samples on an overhead shaker for ~ 24 hours.

SSA was measured on ~ 1 – 4 g aliquots of river sediment using a Quantachrome NOVAtouch LX gas sorption analyser. Before measurement, samples were combusted at 350°C to remove organic matter then degassed to 40 mtorr at 350°C on a Quantachrome FLOWAC degasser to remove excess water. SSA values were calculated from the N_2 adsorption isotherm, following the Brunauer, Emmett and Teller theory⁵².

Acid-extractable metals. To extract the Al, Fe, Mg and Mn ions from the reactive grain coatings of the suspended sediment samples, we used a two-step leaching procedure adapted from Wittmann et al.⁵³. We first dried 0.5–1.0 g sediment aliquots at 110°C overnight. After drying, samples were sealed and weighed immediately upon cooling. Reactive amorphous oxyhydroxide phases were leached with 10 ml 0.5 M HCl solution, with mild shaking at room temperature for 24 hr. Crystalline oxide phases were leached in 10 ml 1 M hydroxylamine–hydrochloride solution ($\text{NH}_2\text{OH} \times \text{HCl}$ in 1 M HCl) in an ultrasonic bath at 80°C for 4 hr, with shaking every 10 min. The leachates were dried completely, treated with aqua regia to destroy matrices and then diluted in 3 M HNO_3 for measurement. Al, Fe, Mg and Mn concentrations were measured via inductively coupled plasma–optical emission spectroscopy. Concentrations were normalized by initial dry sample mass. Measurements of amorphous and crystalline phases were combined to obtain total reactive metal concentrations.

Depth integration and POC fluxes. For each river depth profile, we calculated depth-integrated $\delta^{13}\text{C}_{\text{POC}}$ and $F^{14}\text{C}_{\text{POC}}$ values as the weighted means of the measured values for individual samples. Depth-integrated values were weighted by suspended sediment concentration and POC concentrations (TOC_{POC}) measured for each sampling depth (Supplementary Table 1). We estimated uncertainty as the standard error of the weighted mean.

We quantified the annual fluxes of POC delivered to (Q_{hw}) and exported from (Q_{out}) the mainstem Rio Bermejo as the product of mean annual suspended sediment flux and depth-integrated POC concentration of the suspended sediment. For these calculations, we used the long-term suspended sediment fluxes measured at gauging stations at river km 0 and km 1,086 reported by Repasch et al.⁵⁴ and depth-integrated POC concentrations measured at downstream km 0 and downstream km 1,220 (this study).

***n*-alkane radiocarbon measurements.** We measured compound-specific ^{14}C content of leaf wax *n*-alkanes to trace the radiocarbon signature of vascular plant-derived POC. Lipid compounds were extracted from bulk sediment using a Dionex accelerated solvent extraction system (ASE 350), and the *n*-alkanes were further isolated by solid-phase extraction over silica gel columns following

the manual procedure of Rach et al.⁵⁴. The C_{27} , C_{29} , C_{31} and C_{33} *n*-alkanes were then purified from the saturated lipid fraction using preparative capillary gas chromatography following Eglinton et al.⁵⁵. The purified long-chain *n*-alkanes were transferred to tin capsules using dichloromethane and placed in combusted glass vials. Radiocarbon measurements were made by EA-AMS at ETH Zürich following Haghpor et al.⁵⁶. Sample sizes ranged from 21 to 63 μg . The ^{14}C measurements were corrected using the measured ^{14}C content of process blanks and empty tin capsules.

Bayesian isotope mixing model—MixSIAR. To determine the relative contributions of different OC sources to riverine POC, we used a three-endmember Bayesian isotope mixing model constrained by bulk POC $\delta^{13}\text{C}$ and $F^{14}\text{C}$ data for the endmembers. Input to the model included the mean and standard deviation of measured isotopic values for sample sets of leaf litter ($n = 6$), floodplain sediment⁴⁰ ($n = 51$) and topsoil ($n = 17$) (Extended Data Table 2). We calculated the fractional contribution of each endmember to all suspended sediment sample ‘mixtures’ using the R package MixSIAR⁵⁷. We ran the MixSIAR model with an uninformative prior, making no initial assumptions about the source contributions to the samples. The Markov chain Monte Carlo method was performed with 1×10^6 iterations, burn-in of 5×10^5 iterations, thinning factor of 500 and three chains. For each river sediment sample, this analysis yielded three posterior distributions, which contained the full range of possible fractional contributions of the three OC sources. We calculated the mean and standard deviation of the posterior distribution for each source to obtain the most probable values (Extended Data Table 3). We combined the leaf litter and topsoil values to represent the proportion of POC_{fast} in each sample and used the floodplain sediment values to represent POC_{slow} . We estimated the proportions of these two pools for all suspended sediment samples, and then calculated the depth-integrated mean contributions of POC_{fast} and POC_{slow} at the headwaters, resulting in 0.53 ± 0.17 and 0.47 ± 0.10 , respectively. We calculated the mean annual Q_{hw} of POC_{fast} and POC_{slow} as the product of these values and the mean annual headwater POC flux.

Calculating decomposition rate constants. We calculated a characteristic decomposition rate, k , for POC_{fast} and POC_{slow} . We estimated k for POC_{fast} and POC_{slow} following the method of Torn et al.⁴⁵:

$$k = \frac{\lambda \times F^{14}\text{C}}{1 - F^{14}\text{C}} \quad (5)$$

where λ is the ^{14}C decay constant ($1.21 \times 10^4 \text{yr}^{-1}$) and $F^{14}\text{C}$ is a representative fraction modern value for the POC pool of interest. The turnover time corresponding to the POC pool is simply $1/k$, resulting in short turnover times for fast decomposition rates and long turnover times for slow decomposition rates⁴⁵. By selecting just one characteristic $F^{14}\text{C}$ value to input into equation (5), we assume that the entire POC pool being modelled decomposes at the same rate through time.

To determine the POC_{fast} turnover time, we used radiocarbon data from the Rio Bermejo catchment. Leaf litter samples had a mean $F^{14}\text{C}$ value of 1.00 (Extended Data Table 2), indicating modern carbon and suggesting a turnover time < 50 years. Total ecosystem turnover times were estimated at a global scale by Carvalhais et al.⁴⁶, and the ecosystem turnover time for the subtropical Rio Bermejo region was modelled at ~ 17 years. We used this turnover time to determine a characteristic decomposition rate of 0.06yr^{-1} for POC_{fast} . This is six times faster than, but of the same magnitude as, other estimates made for POC_{bio} in the literature (for example, Torres et al.²³). Where turnover times for POC_{bio} are estimated, mineral-bound POC_{bio} is included in this estimate, while we consider only free, labile POC in the fast-cycling pool.

Validating the modelled lateral POC influx. Balancing the Rio Bermejo carbon budget (equation (4)) revealed that the lateral influx of floodplain POC significantly influences the strength of the carbon sink. We estimated the possible lateral influx of POC into the Rio Bermejo from the floodplain due to lateral channel migration (Q_{lat}) as:

$$Q_{\text{lat}} = m_{\text{lat}} \times L \times \text{NPP} \quad (6)$$

where m_{lat} is the mean lateral channel migration rate (m yr^{-1}), L is the total channel length (m) and NPP is the net primary productivity of floodplain biomass (kgC). Lateral channel migration rates for the Rio Bermejo range from 0 to 30m yr^{-1} , averaging $14.9 \pm 6.2 \text{m yr}^{-1}$. The length of the lowland segment of the Rio Bermejo is 1,267 km. We calculated the mean NPP for the lowland portion of the Rio Bermejo catchment (east of the mountain front) using the MODIS MOD17A3H V6 annual NPP product for the year 2014 (500 m pixel resolution). The mean NPP for the $\sim 70,000 \text{km}^2$ area was $3,623 \pm 4,373 \text{kgC m}^{-2}$. Applying equation (6) gives $Q_{\text{lat}} = 6.84 \pm 2.85 \times 10^4 \text{tC yr}^{-1}$, which agrees well with our model estimate of $4.58 \times 10^4 \text{tC yr}^{-1}$ derived from the equation (4).

Data availability

The data supporting the findings of this study are available at the PANGAEA data repository. Data for Rio Bermejo suspended sediment samples can be accessed at

<https://doi.pangaea.de/10.1594/PANGAEA.925701>. Organic geochemical data for Rio Bermejo topsoil, leaf litter and floodplain sediment can be accessed at <https://doi.pangaea.de/10.1594/PANGAEA.925616>.

References

- Galy, V., Bouchez, J. & France-Lanord, C. Determination of total organic carbon content and $\delta^{13}\text{C}$ in carbonate-rich detrital sediments. *Geostand. Geoanal. Res.* **31**, 199–207 (2007).
- Ruff, M. et al. On-line radiocarbon measurements of small samples using elemental analyzer and MICADAS gas ion source. *Radiocarbon* **52**, 1645–1656 (2010).
- Brunauer, S., Emmett, P. H. & Teller, E. Adsorption of gases in multimolecular layers. *J. Am. Chem. Soc.* **60**, 309–319 (1938).
- Wittmann, H. et al. The dependence of meteoric ^{10}Be concentrations on particle size in Amazon River bed sediment and the extraction of reactive $^{10}\text{Be}/^{9}\text{Be}$ ratios. *Chem. Geol.* **318–319**, 126–138 (2012).
- Rach, O., Hadeen, X. & Sachse, D. An automated solid phase extraction procedure for lipid biomarker purification and stable isotope analysis. *Org. Geochem.* **142**, (2020).
- Eglinton, T. I., Aluwihare, L., Bauer, J. E., Druffel, E. R. M. & McNichol, A. P. Gas chromatographic isolation of individual compounds from complex matrices for radiocarbon dating. *Anal. Chem.* **68**, 904–912 (1996).
- Haghipour, N. et al. Compound-specific radiocarbon analysis by elemental analyzer-accelerator mass spectrometry: Precision and limitations. *Anal. Chem.* **91**, 2042–2049 (2019).
- Stock, B. C. et al. Analyzing mixing systems using a new generation of Bayesian tracer mixing models. *PeerJ* **2018**, 1–27 (2018).

Acknowledgements

We thank M. Strecker for support through the StRATEGy international research training group (Deutsche Forschungsgemeinschaft (DFG) grant STR 373/34-1 (M.R. and D.S.)). We are grateful for assistance from D. Montluçon for compound-specific radiocarbon

and surface-area measurements, the ETH Laboratory of Ion Beam Physics for AMS support, N. Golombek for sample preparation, and R. Szupiany and R. Lopez for field assistance.

Author contributions

M.R., J.S.S., N.Hovius and D.S. designed the study and contributed to data interpretation and model development. M.R. and J.S.S. collected and processed samples, with help from D.S., N.Hovius and H.W. H.W. provided analytical assistance for reactive metal extraction and measurement. M.L., N.Haghipour and T.I.E. provided radiocarbon measurements. D.R.G. provided stable carbon isotope measurements. M.R. analysed the data, produced the figures and authored the manuscript (with significant input from J.S.S., N.Hovius, D.S. and M.L.). All co-authors reviewed, commented on and approved the manuscript.

Funding

Open access funding provided by Helmholtz-Zentrum Potsdam Deutsches GeoForschungsZentrum—GFZ.

Competing interests

The authors declare no competing interests.

Additional information

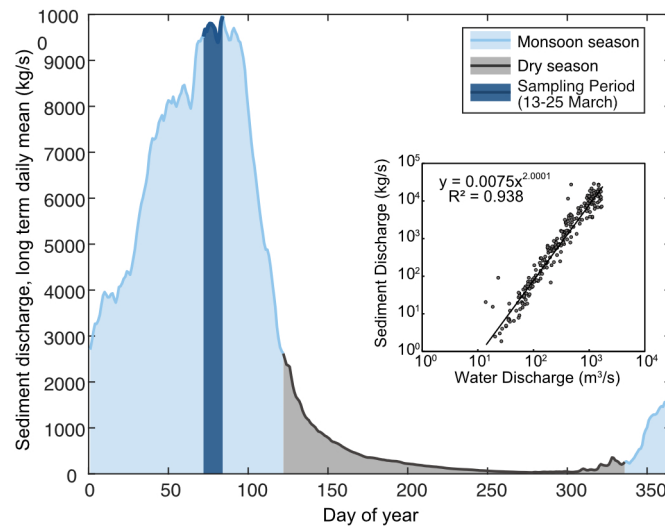
Extended data is available for this paper at <https://doi.org/10.1038/s41561-021-00845-7>.

Supplementary information The online version contains supplementary material available at <https://doi.org/10.1038/s41561-021-00845-7>.

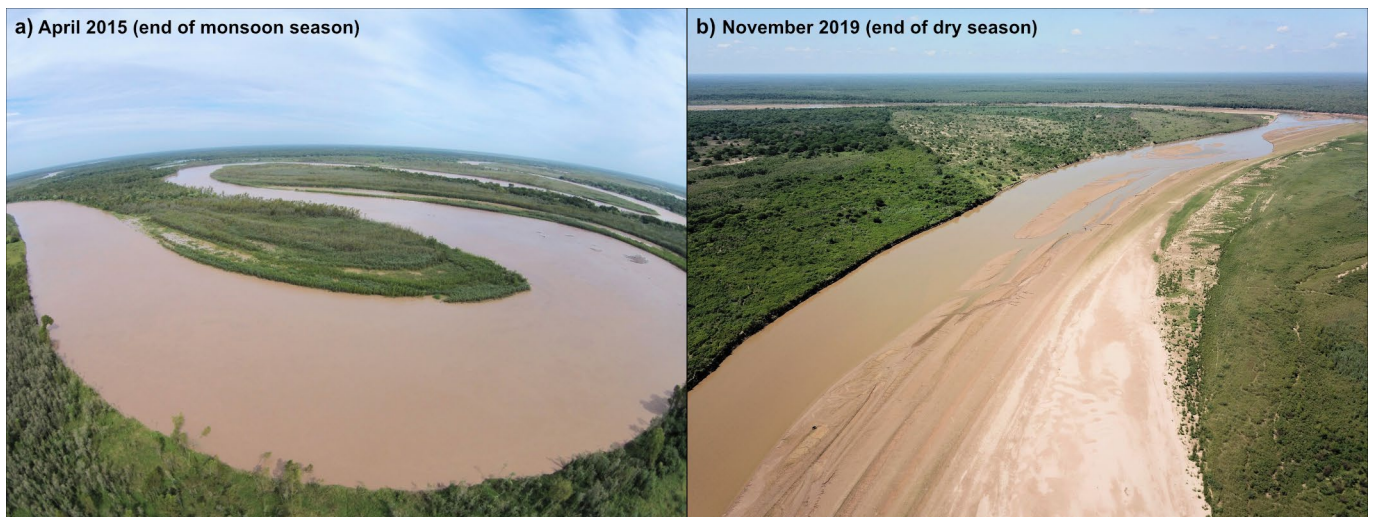
Correspondence and requests for materials should be addressed to Marisa Repasch.

Peer review information *Nature Geoscience* thanks the anonymous reviewers for their contribution to the peer review of this work. Primary Handling Editors: Clare Davis and Simon Harold.

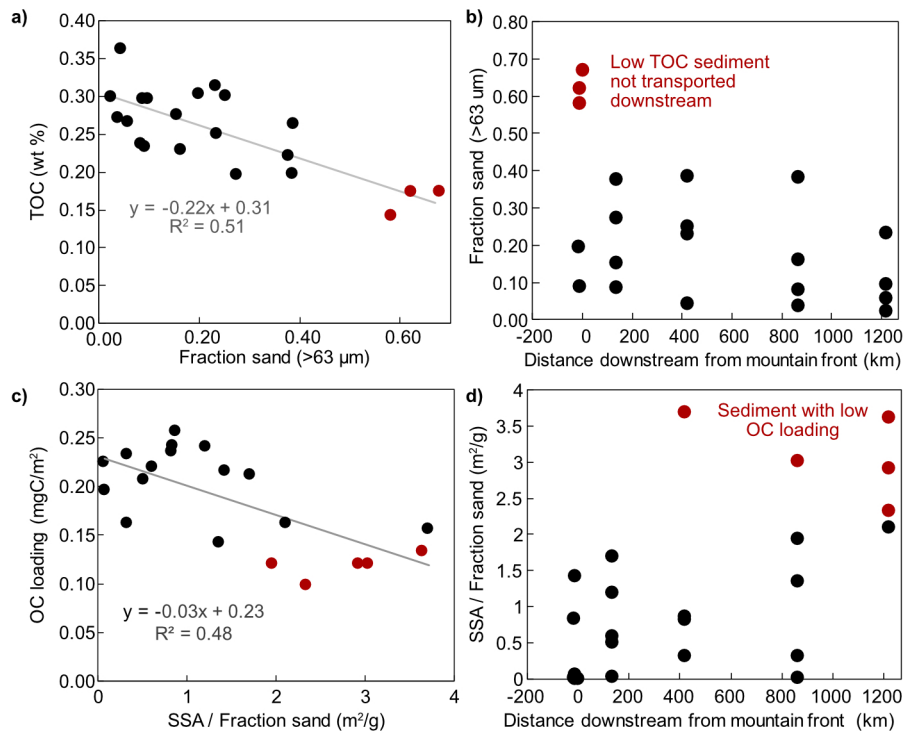
Reprints and permissions information is available at www.nature.com/reprints.



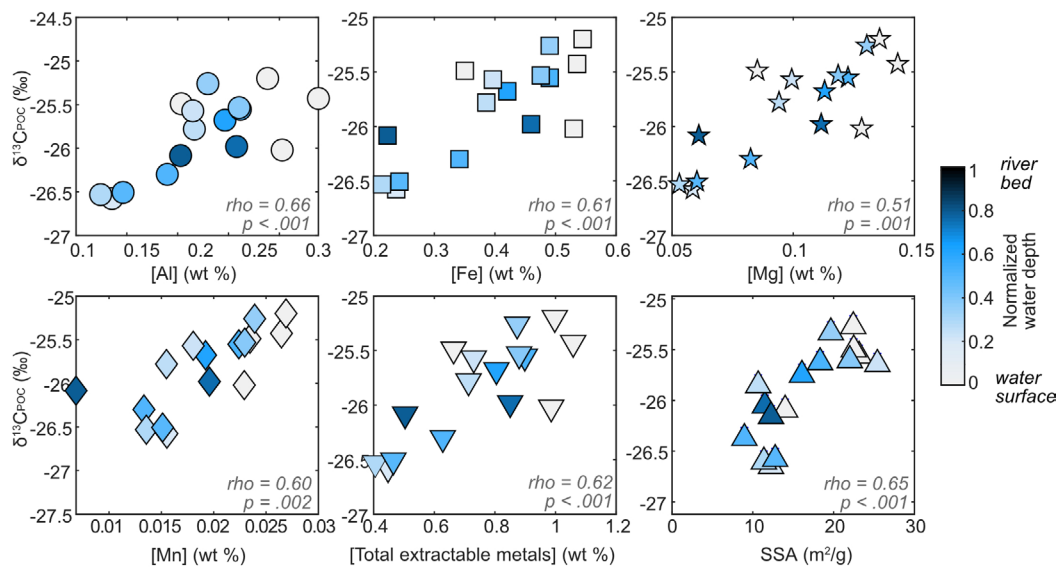
Extended Data Fig. 1 | Long-term mean daily suspended sediment discharge for the Rio Bermejo (averaged over 1970-2016 gauging record at El Colorado, river km 1086). Dark blue shading indicates our sampling period (13-25 March 2017). Inset shows the water discharge-suspended sediment discharge rating curve used to generate the mean sediment flux. Data was downloaded from the Argentina National System of Hydrologic Information (<https://snih.hidricosargentina.gob.ar/>).



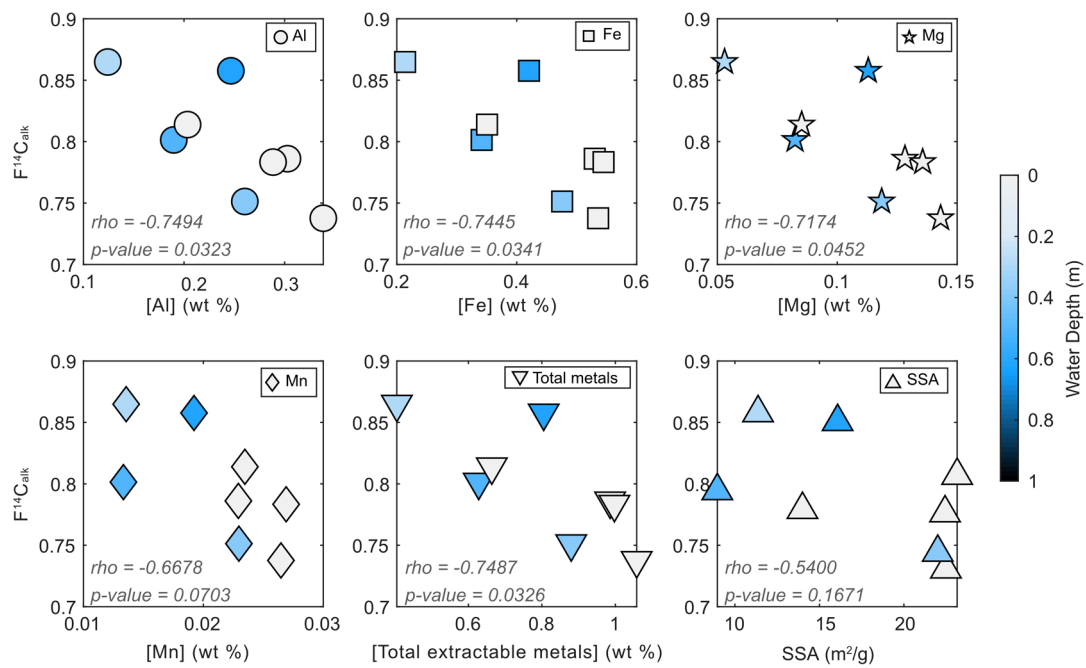
Extended Data Fig. 2 | Aerial photos of the Rio Bermejo showing high turbidity during both high flow and low flow conditions. a) Photo captured near river km 1260 in April 2015 (end of monsoon season). **b)** Photo captured near river km 450 in November 2019 (end of dry season).



Extended Data Fig. 3 | Effects of sediment grain size and specific surface area (SSA) on along-channel changes in POC content and loading. **a)** fraction of sand-sized particles (>63 μm) vs. TOC (weight %), **b)** distance downstream along the channel vs. fraction of sand-sized particles, **c)** Specific surface area (SSA) normalized by fraction of sand-sized particles vs. OC loading, and **d)** distance downstream along the channel vs. SSA normalized by fraction of sand-sized particles.



Extended Data Fig. 4 | Relationships between acid extractable metal concentrations, specific surface area (SSA), and $\delta^{13}\text{C}$ values of organic carbon in suspended sediment samples ($\delta^{13}\text{C}_{\text{POC}}$). Rho is the Pearson correlation coefficient, and the p-value indicates the statistical significance of those relationships.



Extended Data Fig. 5 | Relationships between acid extractable metal concentrations, specific surface area (SSA), and $F^{14}C$ values of C27, C29, C31, and C33 *n*-alkanes in suspended sediment samples ($F^{14}C_{alk}$). Rho is the Pearson correlation coefficient, and the *p*-value indicates the statistical significance of those relationships.

POC Source	Mean $\delta^{13}\text{C}$	SD $\delta^{13}\text{C}$	Mean F^{14}C	SD F^{14}C	n
Topsoil	-24.41	3.63	1.00	0.06	17
Floodplain sediment	-22.17	2.94	0.77	0.15	51
Leaf litter	-25.68	4.37	0.98	0.01	6

Extended Data Table 1 | Mean isotopic values of POC sources floodplain sediment, topsoil, and leaf litter samples within the catchment. SD = standard deviation of the mean \Means and standard deviations are derived from sets of topsoil, floodplain sediment⁴⁰, and leaf litter samples collected throughout the catchment.

Sample Name	Fraction floodplain ^a	Fraction leaf litter ^a	Fraction topsoil ^a	POCfast ^b	POCslow
AR17MR-31	0.44 ± 0.09	0.38 ± 0.14	0.19 ± 0.14	0.56 ± 0.20	0.44 ± 0.09
AR17MR-24	0.54 ± 0.17	0.29 ± 0.17	0.17 ± 0.16	0.46 ± 0.23	0.54 ± 0.17
AR17MR-25	0.50 ± 0.17	0.32 ± 0.17	0.18 ± 0.17	0.50 ± 0.25	0.50 ± 0.17
AR17MR-26	0.42 ± 0.17	0.37 ± 0.20	0.21 ± 0.20	0.58 ± 0.28	0.42 ± 0.17
AR17MR-32	0.44 ± 0.17	0.35 ± 0.19	0.21 ± 0.19	0.56 ± 0.27	0.44 ± 0.17
AR17MR-33	0.27 ± 0.16	0.51 ± 0.24	0.23 ± 0.22	0.73 ± 0.33	0.27 ± 0.16
AR17MR-34	0.32 ± 0.17	0.45 ± 0.22	0.23 ± 0.22	0.68 ± 0.31	0.32 ± 0.17
AR17MR-35	0.30 ± 0.16	0.47 ± 0.23	0.23 ± 0.22	0.70 ± 0.31	0.30 ± 0.16
AR17MR-11	0.56 ± 0.16	0.28 ± 0.16	0.16 ± 0.15	0.44 ± 0.22	0.56 ± 0.16
AR17MR-12	0.44 ± 0.17	0.36 ± 0.19	0.20 ± 0.19	0.56 ± 0.27	0.44 ± 0.17
AR17MR-13	0.62 ± 0.15	0.24 ± 0.14	0.15 ± 0.14	0.38 ± 0.20	0.62 ± 0.15
AR17MR-14	0.35 ± 0.17	0.42 ± 0.22	0.23 ± 0.21	0.65 ± 0.30	0.35 ± 0.17
AR17MR-42	0.40 ± 0.17	0.38 ± 0.20	0.21 ± 0.20	0.60 ± 0.29	0.40 ± 0.17
AR17MR-43	0.41 ± 0.17	0.38 ± 0.20	0.22 ± 0.20	0.59 ± 0.28	0.41 ± 0.17
AR17MR-44	0.41 ± 0.17	0.39 ± 0.20	0.21 ± 0.20	0.59 ± 0.29	0.41 ± 0.17
AR17MR-45	0.42 ± 0.17	0.36 ± 0.20	0.21 ± 0.20	0.58 ± 0.28	0.42 ± 0.17
AR17MR-05	0.31 ± 0.17	0.46 ± 0.23	0.23 ± 0.21	0.69 ± 0.31	0.31 ± 0.17
AR17MR-06	0.44 ± 0.17	0.35 ± 0.19	0.20 ± 0.19	0.56 ± 0.27	0.44 ± 0.17
AR17MR-07	0.50 ± 0.17	0.31 ± 0.18	0.19 ± 0.18	0.50 ± 0.25	0.50 ± 0.17
AR17MR-08	0.48 ± 0.16	0.33 ± 0.18	0.19 ± 0.18	0.52 ± 0.26	0.48 ± 0.16
Mean at river km 0 ^c				0.53 ± 0.17	0.47 ± 0.10

Extended Data Table 2 | Mixing model results representing the fraction of floodplain OC, leaf litter OC, and topsoil OC in each suspended sediment sample. ^auncertainty reported as standard deviation of MixSIAR posterior distributions ^bPOCfast = fraction leaf litter + fraction topsoil ^cweighted mean of AR17MR-31, 24, 25, and 26, weighted by suspended sediment concentration; uncertainty reported as standard error of the weighted mean.

C pool	F ¹⁴ C	λ 1/yr	τ yr	k 1/yr	source
POC _{slow}	0.740	1.21E-04	2905	4.00E-04	this study
POC _{fast}	0.998	1.21E-04	17	6.00E-02	Carvalhais et al. 2014

Extended Data Table 3 | Radiocarbon data used to estimate decomposition rates for POC_{slow} and POC_{fast}. $\lambda = 14\text{C}$ decay constant (1.21×10^{-4}) $\tau =$ organic carbon turnover time $k =$ organic carbon decomposition rate.

	Distance along channel	Reach length	Mean transit time through reach	Mean sediment velocity	Sediment deposition-erosion cycles	Turnover length scale POC _{slow} ^a	Turnover length scale POC _{fast} ^a	Number of POC _{slow} turnover cycles ^a	Number of POC _{fast} turnover cycles ^a	POC _{slow} total turnover ^b	POC _{fast} total turnover ^b	POC _{slow} oxidation flux ^b	POC _{fast} oxidation flux ^b
	km	km	yr	km/yr		km	km			MtC	MtC	tC/yr	tC/yr
Reach 1	0 - 135	135	350 ± 270	0.39 ± 0.17	0.50	953 ± 415	6.43 ± 2.80	0.12 ± 0.04	21.0 ± 6.36	0.01 (+0.01/-0.01)	2.33 (+1.48/-1.08)	29.5 (+22.9/-16.4)	5880 (+4240/-3100)
Reach 2	135 - 422	287	490 ± 180	0.59 ± 0.16	1.70	1450 ± 388	9.77 ± 2.62	0.17 ± 0.04	29.39 ± 6.21	0.01 (+0.01/-0.01)	3.26 (+1.73/-1.34)	29.6 (+19.2/-14.7)	5880 (+3530/-2730)
Reach 3	422 - 866	444	4490 ± 100	0.10 ± 0.00	3.37	244 ± 5.56	1.65 ± 0.04	1.52 ± 0.03	269 ± 5.98	0.13 (+0.05/-0.05)	29.9 (+9.24/-8.86)	29.5 (+11.6/-11.1)	5880 (+2060/-1970)
Reach 4	866-1221	355	3190 ± 490	0.11 ± 0.02	3.88	274 ± 37.0	1.85 ± 0.25	1.09 ± 0.13	192 ± 22.8	0.10 (+0.05/-0.04)	21.30 (+8.99/-7.56)	29.6 (+15.5/-13.0)	5900 (+2820/-2370)
Averaged over full river length	0 - 1267	1267	8520 ± 596	0.15 ± 0.07	4.50	358 ± 161	2.42 ± 1.08	2.97 ± 0.92	524 ± 162	0.26 (+0.20/-0.14)	58.2 (+37.5/-27.3)	30.4 (+23.8/-17.0)	6050 (+4410/-3210)

Extended Data Table 4 | Organic carbon turnover estimates for the Rio Bermejo. ^aUncertainty propagated from sediment transit velocity ^bUncertainty represents maximum and minimum range propagated from sediment transit time and mixing model uncertainties.